

Magnetic circuit design of high-power Hall thruster

Zihan Tu¹, Yanlin Hu¹, Wei Mao¹, Chao Hou¹, Nan Wu¹

¹Beijing Engineering Research Center of Efficient and Green Aerospace Propulsion Technology
Beijing Institute of Control Engineering, Beijing, China; Beijing Institute of Control Engineering, Beijing, China

Abstract: High-power Hall thrusters constitute a prominent propulsion method for contemporary deep space exploration missions, yet there remains a scarcity of models adequately suited for space applications. The magnetic circuit of a Hall thruster plays a pivotal role in shaping the magnetic field configuration within the discharge chamber, thereby influencing the thruster's performance. This paper aims to undertake the design of a magnetic circuit for a high-power Hall thruster, initiating from a thoroughly flight-validated medium-power model. Employing scaling methods, a preliminary magnetic circuit for a 10 kW high-power Hall thruster is designed. Leveraging previously established high-efficiency and high-quality magnetic circuit optimization techniques, an optimized magnetic circuit is attained, resulting in a 24.6% reduction in magnetic circuit mass, a decrease in the magnetic tilt angle from beyond 20° to within 6°, a 10.5% increase in maximum magnetic field strength, and a 19.6% enhancement in magnetic field gradient. The magnetic circuit design for the 10 kW thruster is accomplished, with the projected thrust increase reaching 480% and specific impulse improvement by 20%. The magnetic circuit, designed using finite element methods to precisely match magnetic field requirements, has demonstrated favorable outcomes, validating the effectiveness of the approach.

Keywords: electric propulsion technology, Hall thrusters, finite element analysis, optimization design

1 Introduction

Since the implementation of an all-electric propulsion platform with the PPS-1350 thruster on the SMART-1 spacecraft^[1-2], the adoption of such platforms has become one of the key indicators of satellite sophistication. Among electric propulsion systems, Hall thrusters, classified as electrostatic thrusters, have garnered widespread application across various space missions due to their simplicity in design, high thrust density, and moderate specific impulse^[3-8]. As the scope and depth of space exploration continue to expand, high-power electric propulsion has emerged as a pivotal strategic direction in the international arena of advanced space propulsion technologies^[9].

Hall thrusters can be categorized into high, medium, and low-power classes according to their operating power range, with medium power typically ranging from 1 to 5 kW and anything above 5 kW classified as high-power^[10]. Compared to the medium-power Hall thrusters that have already been widely employed in actual space missions^[11-18], high-power thrusters exhibit greater adaptability to mission requirements, excelling particularly in deep space exploration, orbit transfer, and tasks demanding high-energy efficiency and long-term stability. Many high-power thrusters allow for a switch between high-thrust and high-specific impulse modes by adjusting discharge voltage and propellant flow rate, enabling swift orbit transfers with high thrust or conserving propellant with high efficiency during attitude control and station-keeping operations. Historically, space missions focused on near-Earth orbits, but with the growing demands of space exploration, deep space missions such as Mars and

lunar exploration have become increasingly significant. These endeavors necessitate propulsion systems with prolonged operational capability, high specific impulse, efficient thrust, and minimal mass. High-power Hall thrusters maintain high efficiency while offering greater specific impulse and thrust, thereby addressing the limitations of medium-power units in deep space missions^[19-27]. The magnetic circuit of a Hall thruster significantly influences the magnetic field configuration within the discharge channel, a critical aspect that directly impacts plasma focusing, plume divergence, and electron dynamics. Advancements in magnetic circuit design facilitate precise magnetic field control, which in turn enhances the performance, efficiency, longevity, and stability of the Hall thruster.

Both domestic and international research communities have embarked on studies and developed representative models of high-power thrusters. Among them, the SPT-200 is a non-magnetically shielded thruster designed for a power of 12 kW, featuring a mechanical structure that distributes thermal loads, enhanced fluid and electrical interfaces, and a centrally mounted, cathode neutralizer without a heater^[20]. However, given its earlier design, the SPT-200 suffers from lower efficiency, excessive weight, and severe wall erosion that limits its lifespan. The BHT-8000, with a design power of 8 kW, also non-magnetically shielded, has demonstrated the feasibility of utilizing diverse propellants such as xenon, krypton, and iodine^[21]; nonetheless, it faces challenges including longer ignition times, shorter operational lives, and higher noise levels. Building upon this, the BHT-20k was developed, achieving a higher power level (20 kW), greater thrust (1 N), and superior performance (specific impulse of 2500 s and efficiency of 69%)^[22]. At the forefront of high-power Hall thrusters are models like the American 20 kW-class NASA-300M, distinguished by its high efficiency (68%) and specific impulse (2820 s), with an impressive in-orbit lifetime exceeding 10,000 hours. The NASA-173Mv2 is an upgraded version of the NASA-173Mv1, with a focus on optimizing the magnetic circuit and enhancing magnetic field symmetry^[23-24], attaining a higher level of technological maturity and highlighting the potential for substantial performance improvements through magnetic field optimization^[25]. Another milestone is the HERMeS thruster from the U.S., which employs magnetic shielding technology to mitigate the severe wall erosion caused by high-energy ions in conventional high-power thrusters, significantly enhancing thruster longevity, and marking a crucial step forward in high-power Hall thruster technology^[26-27].

Currently, countries around the globe are actively engaged in the research and development of high-power Hall thrusters, highlighting their significant application potential and vast prospects for advancement. However, the limited use of high-power models in actual space missions suggests that the technology's maturity level is not yet sufficiently high, with design challenges yet to be fully overcome. High-power Hall thrusters impose stricter demands on the intensity, gradient, and topology of magnetic fields, thereby complicating the task of tuning and matching magnetic circuits. Undertaking the design of magnetic circuits for high-power Hall thrusters is instrumental in addressing some of the existing developmental issues, contributing to optimized magnetic field distributions, enhanced efficiency and stability, adaptability to a broader range of operating conditions, and prolonged operational life. This paper initiates from Hall thrusters that have undergone extensive in-flight validation at medium thrust levels and employs scaling methods to devise an initial magnetic circuit design. Subsequently, leveraging the previously established methodology for Hall thruster magnetic circuit design based on dimensional optimization^[28], adjustments to the magnetic circuit are carried out. Ultimately, a refined magnetic circuit design for a 10 kW-class high-power Hall thruster is accomplished, yielding favorable outcomes.

2 Hall Thruster Magnetic Circuit Design

2.1 Magnetic field calculation

After the Hall thruster operates stably, the excitation power remains constant. The equation for calculating the magnetic field in the discharge channel is the steady-state Maxwell's equations, and the expression is as follows:

$$\begin{cases} \nabla \times H = J \\ B = \mu H \\ \nabla \cdot B = 0 \\ B = \nabla \times A \end{cases} \quad (1)$$

Among them, μ represents magnetic permeability, A represents magnetic vector potential, B represents magnetic induction intensity, H represents magnetic field intensity, J represents electrical conductivity.

In cylindrical coordinate system, considering only the θ component in axisymmetric systems, this component is a function of r and z , which can be expressed as

$$\begin{cases} A = A_\theta(r, z)e_\theta \\ J = J_\theta(r, z)e_\theta \end{cases} \quad (2)$$

In conclusion, the magnetic field calculation equation for the Hall thruster model is obtained

$$\begin{cases} \frac{\partial}{\partial r} \left[\frac{1}{\mu r} \frac{\partial}{\partial r} (rA_\theta) \right] + \frac{\partial}{\partial z} \left(\frac{1}{\mu} \frac{\partial A_\theta}{\partial z} \right) = -J_\theta \\ B_r = -\frac{\partial A_\theta}{\partial z} \\ B_\theta = 0 \\ B_z = \frac{1}{r} \frac{\partial}{\partial z} (rA_\theta) \end{cases} \quad (3)$$

Regarding boundary treatment, it is assumed that all boundaries are magnetic insulating boundaries, which means $n \times A = 0$.

In addition, when there is a ferromagnetic material present in the computational domain, the calculation formula for magnetic field intensity is modified as

$$B = \mu_0 \mu_r H \quad (4)$$

Where μ_0 represents vacuum permeability, μ_r represents relative magnetic permeability of the material. The value of μ_r depends on the magnetization curve of the material and is also related to the magnetic field intensity B in the actual calculation, so the magnetic field calculation is an iterative process.

2.2 Determination of magnetic circuit form

Fundamentally, the core objective of Hall thruster magnetic circuit design is to establish a stable magnetic field within the discharge channel, characterized by a strength and geometry that effectively traps electrons in both the ionization and acceleration zones. This confines electron flow along the axial direction, compelling them to circulate radially where they ionize the propellant. The resultant magnetic field must also efficiently accelerate ions, ensure effective plasma beam focusing, and minimize wall erosion, all in alignment with specified thrust, specific impulse, and efficiency requisites. The initial magnetic circuit configuration adopted

here is the widely employed dual-magnetic shield design, whose intricacies were elaborated upon in a patent by American scholar MANZELLA et al. [29] (depicted in Figure 1). This architecture effectively satisfies multiple criteria for magnetic field structure, gradient, and intensity, facilitating the adjustment of magnetic parameters. Moreover, it confers advantages such as prolonged thruster lifespan, rendering it the prevalent choice for the majority of high-power Hall thrusters [19-27].

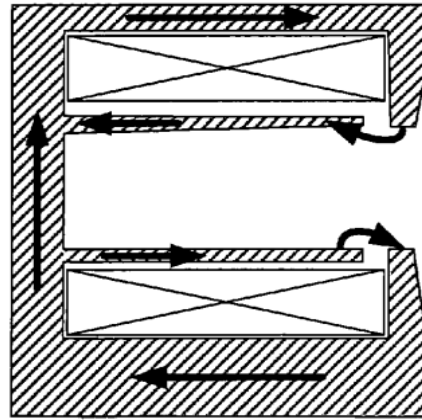


Fig.1 A typical magnetic circuit structure with double magnetic screens

Once the configuration of the magnetic circuit is established, the subsequent challenge lies in defining the dimensions and placement of the discharge channel, effectively determining the operational reach of the magnetic circuit design. The dimensions of the discharge channel, encompassing the average diameter of the thruster, channel length, width, and shape, significantly influence performance aspects such as ionization efficiency and thrust efficiency. For instance, the channel width affects the flow area and particle collisions with the walls; widening the channel can enhance wall surface area and electronic conductivity, reducing electron accumulation and thereby minimizing energy losses and improving operational stability. Conversely, excessively broad channels may reduce the efficiency of energy conversion between electrons and ions. Conversely, narrowing the channel can intensify magnetic confinement, decrease the likelihood of high-energy ion wall impacts, minimize sputter erosion, and prolong thruster lifespan. Furthermore, the discharge channel influences the thermal distribution and thermal stability of the thruster. Taking into account the mechanisms by which the discharge channel impacts thruster performance and the practical requirements of magnetic circuit design, this paper selects three parameters as characteristic dimensions: the average radius of the discharge channel R (defining its central position), the channel length L , and the channel width W . These dimensions are meticulously chosen to optimize the thruster's overall capabilities.

Figure 2 illustrates the finite element model of the Hall thruster, where the black solid lines represent the magnetic circuit and the energizing coils are highlighted by bold, rectangular frames. The entire model is situated within an air domain to ensure ample penetration of magnetic flux lines. Determination of the characteristic dimensions of the discharge channel is primarily linked to the design power and operational conditions of the thruster. This work adopts scaling design methodologies to ascertain these dimensions.

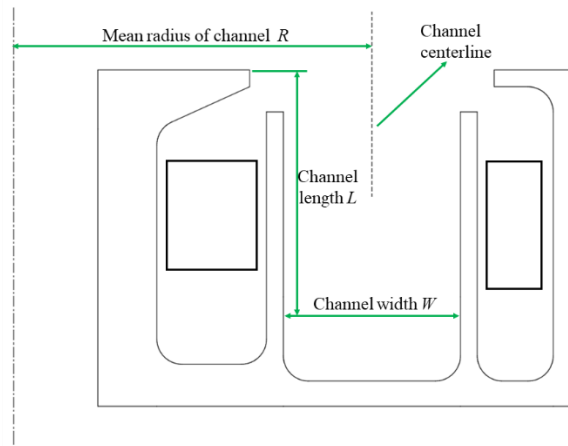


Fig.2 Initial magnetic circuit and feature length diagram

2.3 Hall thruster scaling design method

In embarking on the magnetic circuit design for high-power Hall thrusters, initiating the design process from scratch would necessitate intricate physical modeling investigations and extensive experimental testing, a path that is both time-consuming and resource-intensive. Existing Hall thrusters, having undergone prolonged refinement and improvement, exhibit a well-balanced physics regime, furnishing an ideal blueprint for design. By scaling up the dimensions of proven, mid-power thrusters through established methodologies, the development cycle can be significantly truncated, costs reduced, and the iterative exploratory phase circumvented, thereby mitigating uncertainties and potential technological risks inherent in the design process. Consequently, this study intends to select a reference thruster, one that has undergone comprehensive flight validation, from the existing repertoire of Hall thrusters. Leveraging the dimensions of this reference thruster, an initial magnetic circuit scale for the high-power variant will be determined via scaling techniques. Central to this scaling approach is the preservation of consistency in the internal physical processes, chiefly by maintaining the propellant density n_n , a strategy validated $n_n = 1.3 \times 10^{19} m^{-3}$ to facilitate stable thruster operation and the attainment of high efficiencies [30-31].

The crux of employing scaling methods lies in establishing the scaling ratios among various parameters. Drawing from the corpus of scholarly research [30-34], determining channel dimensions based on power levels requires delineating the relationships between characteristic parameters (such as average diameter, channel width, and channel length) and performance metrics including power, specific impulse, discharge voltage, and thrust.

Specifically, Draren Yu et al. [32], approaching the issue from the perspective of propellant ionization, elucidate an underlying relationship between the mean free path of ionization within the Hall thruster and the channel length, highlighting a critical interplay that governs the internal dynamics of the thruster:

$$\lambda_i / L \equiv \text{Cons} \quad (5)$$

Where the mean free path of ionization [1] can be represented as:

$$\lambda_i = \frac{v_n(T_n)}{n_n \sigma_i(T_e) v_e(T_e)} \quad (6)$$

Parentheses indicate the presence of an implicit functional relationship.

According to the findings by researchers such as V. Zhurin [33] and M. Martinez-Sanchez [34], the electron number density [1], atomic number density [2], and channel length [3] within the conduit are related as follows:

$$n_e \propto \frac{1}{L} \quad (7)$$

$$n_n \propto \frac{1}{L} \quad (8)$$

K. Dannenmayer^[31] deduced the aforementioned relationships from the perspective of working fluid mass flow rate \dot{m}_n :

$$n_n \propto \frac{\dot{m}_n}{WR} \quad (9)$$

where R denotes the average radius

The relationship between the magnetic field B and the channel dimensions is as follows:

$$B \propto \frac{\sigma_{en}(T_n, T_e) v_e(T_e)}{v_n(T_n)} \frac{\dot{m}_n}{WR} \quad (10)$$

where σ_{en} represents the area of electron-atom kinetic energy exchange

The relationship between thrust T and channel dimensions is as follows:

$$T \propto \alpha \gamma \theta_d v_n(T_n) \frac{1}{L} \sqrt{U_d - \Delta} WR \quad (11)$$

where α is the ionization efficiency factor, γ is the average correction factor for multi-charged ions, θ_d is the plume divergence correction factor, v_n and T_n respectively denote the atomic thermal velocity and atomic temperature, and Δ represents voltage loss.

The relationship between the thruster power P and channel dimensions is as follows:

$$P = U_d I_d \propto \gamma' \alpha v_n(T_n) \frac{WR}{L} U_d \quad (12)$$

The specific impulse I_{sp} is directly correlated solely with the discharge voltage, with the relationship being as such:

$$I_{sp} = \frac{T}{\dot{m}_n g_0} \propto \sqrt{U_d - \Delta} \quad (13)$$

There is no direct correlation between the efficiency η_T of the thruster and the channel dimensions:

$$\eta_T = \frac{T^2}{2\dot{m}P_{in}} \propto \alpha \theta_d^2 \frac{\gamma^2}{\gamma'} \frac{U_d - \Delta}{U_d} \neq f(W, R, L) \quad (14)$$

Equations (5) through (14) illustrate the relationships between thruster performance parameters and the characteristic dimensions of the channel. However, the physical processes within the Hall thruster's channel during operation are considerably complex. To ascertain scaling factors, the following assumptions must be made: all quantities are time-independent; the electron temperature T_e remains constant and uniform under any operating condition; the propellant gas exhibits a uniform and fixed temperature T_n throughout the channel, hence its velocity due to free thermal motion v_n is also constant; potential energy is fully converted to kinetic energy, with all ions experiencing the entire potential drop, neglecting voltage losses; plasma-wall interactions are regarded as a thermal load on the channel walls; electron transport across magnetic barriers is considered via classical models, disregarding anomalous transport in high magnetic field regions; multiple charged ions in the plasma are neglected; a collimated plume is produced, implying zero plasma jet divergence; and particle number density within the channel is maintained constant. Simplifying these assumptions yields the following proportional relationships for thrust existence, with T_1 and T_2 representing two distinct proportional dependencies

for thrust.

$$P \propto U_d R^2 \quad (15)$$

$$T_1 \propto \dot{m} \sqrt{U_d} \quad (16)$$

$$T_2 \propto \sqrt{U_d} R^2 \quad (17)$$

$$I_{sp} \propto \sqrt{U_d} \quad (18)$$

$$L \propto \lambda_i \quad (19)$$

$$W \propto R \quad (20)$$

Where Equations (17) through (18) are valid under the premise that the propellant density ^[1] remains unchanged.

The process outlined herein for scaling from medium-power to high-power thrusters involves the following steps:

1. Establish the target thruster's discharge voltage and power classification;

2. Obtain the corresponding mean radius (or diameter), designated as $\frac{R}{R_0} = \sqrt{\frac{U_d/U_{d,0}}{P/P_0}}$, based on Equation

(15);

3. Determine the appropriate channel width, identified as $\frac{W}{W_0} = \frac{R}{R_0}$, according to Equation (20).

The crux of scaling the channel length L revolves around maintaining a constant ratio between the channel length and the mean free path for ionization collisions, which, under the assumption of unaltered plasma density and disregard for various losses, remains invariant and thus challenging to ascertain. Factoring in considerations like ion extraction, transitioning to a high-power Hall thruster necessitates proportionate increases in both the ionization and acceleration zones, thereby mandating a longer channel. Consequently, this paper adopts a geometrically similar approach to determine the channel length, implying that the magnification factor for the channel length aligns with that of its width.

2.4 Magnetic circuit optimization design method

Once the characteristic dimensions are established, the magnetic circuit design can commence. A prior study on magnetic circuit optimization has laid the groundwork for a design methodology based on dimension optimization for Hall thrusters, verifying that this approach can automatically accomplish the task of magnetic circuit optimization, accommodating a broad range of varying magnetic field requirements and adjusting multiple critical dimensions of the magnetic circuit simultaneously. This optimization effectively caters to the magnetic field needs of diverse thruster configurations ^[28]. Herein, we provide a concise outline of the pivotal steps involved in this magnetic circuit optimization design method.

Initially, in identifying the optimization variables for the magnetic circuit, the focus is twofold: ensuring the comprehensiveness of variables to cover all magnetically influential dimensions while minimizing their number to uphold optimization efficiency. It is imperative to acknowledge that the magnetic circuit design envelops the discharge channel with magnetic materials, necessitating ample space reservation for the discharge channel. In other words, post-definition of the characteristic dimensions, geometrical constraints come into play,

dictating that adjustments to magnetic circuit variables must not infringe upon the designed clearance of the discharge channel. Consequently, the chosen primary dimensional variables include the height and thickness (x_1 , x_2 , x_3 , x_4) of the magnetic shields, alongside the length and width (x_5 , x_6 , x_7 , x_8 , x_9) of the magnetic poles. Additionally, recognizing their substantial impact on the magnetic circuit's mass, the thicknesses of the inner and outer walls (x_{10} , x_{11}) are incorporated as variables. A graphical depiction of these specific size optimization variables is illustrated in Figure 3.

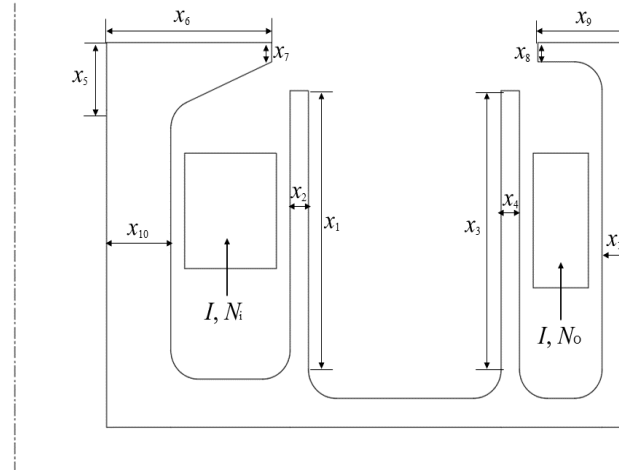


Fig.3 Magnetic circuit optimization variable

Secondly, the mass of the magnetic circuit accounts for over half of the total mass of the thruster, making weight reduction of the magnetic circuit critical for overall thruster lightweighting [35]. Thus, the lightest possible magnetic circuit mass is set as the objective. The dimension-based magnetic circuit design method is essentially a multi-constraint optimization, incorporating magnetic field requirements in various aspects into the optimization process through constraint imposition. These include six specific constraints: magnetic inclination θ , magnetic field gradient ∇B (approximated as $\nabla B = \frac{B_r(\max)}{2\Delta w}$, with Δw representing the half-width of the strong magnetic field region), magnetic field strength in the near-anode region B_0 , maximum magnetic field strength $B_r(\max)$, $B_r(\max)$ axial position $L - B_m$, and material magnetic saturation limits B_{sat} . The summary of these constraints and their corresponding magnetic field demands is presented in Table 1.

TABLE 1 Constraint Settings and definitions

Constraint	Definition	Corresponding magnetic field requirements
Symmetry	θ	Topology
Magnetic field gradient	$\nabla B = \frac{B_r(\max)}{2\Delta w}$	Gradient
Magnetic field strength near the anode	B_0	Gradient Topology
maximum magnetic field strength	$B_r(\max)$	Intensity
The axial position of $B_r(\max)$	$L - B_m$	Intensity
Magnetic saturation	B_{sat}	—

Finally, the optimization algorithm selected is the Nelder-Mead, which is a relatively mature method used for finding the extremum of multidimensional functions. It has been verified to efficiently identify the global optimum solution in magnetic circuit optimizations and meets the requirement of adjusting variables over a wide range. This algorithm has proven to deliver satisfactory results.

The workflow for the magnetic circuit design of a Hall thruster is illustrated in Figure 4. The process begins with specifying the magnetic field requirements and power for the target thruster. An appropriate scaling method is then adopted to determine the characteristic dimensions R , L , and W for the channel design. Following this, the initial magnetic circuit is established based on the chosen magnetic circuit structure. Finally, the optimized magnetic circuit is derived using a finite element-based magnetic circuit design method, thus completing the magnetic circuit design phase.

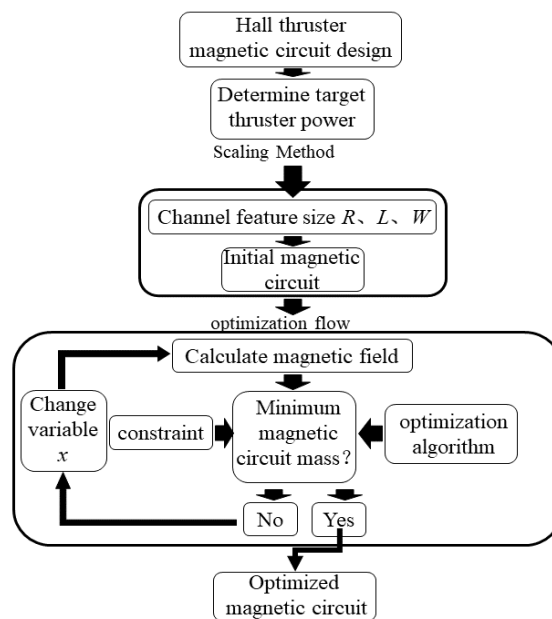


Fig.4 Hall thruster magnetic circuit design flow chart

3 Magnetic Circuit Design of High-power Hall Thruster

3.1 Determination of characteristic size and initial magnetic circuit of high-power Hall thrusters

This paper aims to undertake the magnetic circuit design work for a high-power Hall thruster, targeting a 10kW Hall thruster. Following the workflow for Hall thruster magnetic circuit design, after determining the target power level of 10kW for the thruster, the next step involves channel design and the determination of magnetic circuit characteristic dimensions. This stage makes use of the scaling methods for Hall thrusters.

According to the steps of the scaling method, the first requirement is to select a reference thruster. The PPS-1350, developed by the French company SNECMA, is one of the widely researched and tested Hall thrusters, and has been practically applied in numerous satellites, including the SMART-1 lunar probe. It has accumulated a wealth of practical operational experience and engineering data. Due to its extensive research coverage, practical application background, detailed data records, and the universality provided by its medium power level, this paper selects the PPS-1350 as the reference thruster. The PPS-1350 has a rated power of 1.5kW, with an average radius, channel width, and channel length. Its initial magnetic circuit and characteristic dimensions are marked as shown in Figure 5^[15-18,35-38]. Under nominal operating conditions, the discharge voltage is 350V,

and the discharge current is 4.28A.

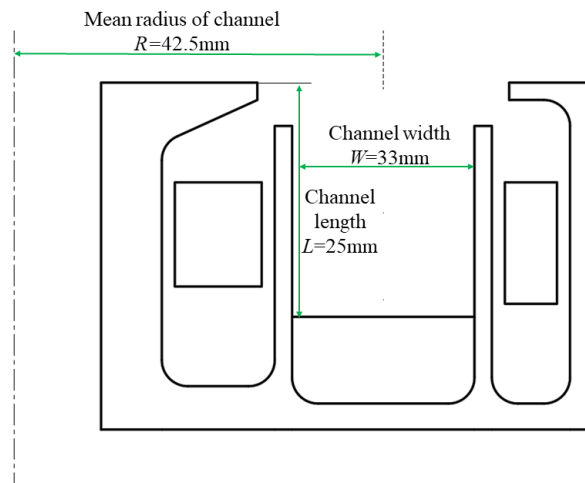


Fig.5 PPS-1350 magnetic circuit structure form and feature size diagram

K. Dannenmayer^[31] remarks that for high-power Hall thrusters in the 10 to 30 kW range, the discharge voltage $U_d = 500V$ can adequately govern secondary electron emission, meeting design specifications. Hence, the power scaling factor $\lambda_p = P / P_0 = 10 / 1.35 = 6.6$ and the discharge voltage scaling factor $\lambda_u = U / U_0 = 500 / 350 = 1.4$ are determined.

Substituting $\lambda_p = 6.6$ and $\lambda_u = 1.4$ into Equation (15) yields $\lambda_r^2 = \left(\frac{R}{R_0}\right)^2 = \frac{\lambda_p}{\lambda_u}$, which equates to $\lambda_R = R / R_0 = 2.2$. Equation (20) informs us that $\lambda_w = W / W_0 = \lambda_R = 2.2$. For the channel length L , a geometric scaling approach is adopted, setting it at $\lambda_L = 2.2$. Under geometric similarity, all other dimensions are scaled up by approximately 2.2 times, with coil dimensions also enlarged to about 2.2 times their original sizes. Assuming a wire diameter of 1.5mm, the upper limit winding counts for the inner and outer coils are calculated to be $N_{in,max} = 364$, $N_{out,max} = 240$. The initial magnetic circuit dimensions after scaling for a target power of 10 kW are depicted in Figure 6.

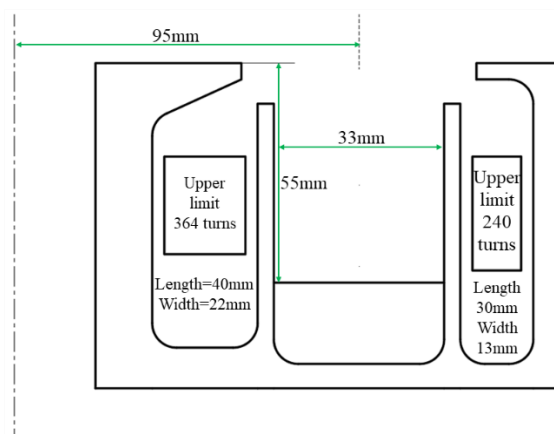


Fig.6 Schematic diagram of the initial magnetic circuit of the 10kW Hall thruster

Aside from the features sizes expanded via scaling methods, other components of the magnetic circuit are derived by enlarging the reference magnetic circuit of PPS-1350 using the same scaling ratio as that applied to the channel dimensions. Detailed dimensions of the PPS-1350 magnetic circuit segments may not have been

publicly disclosed due to confidentiality or similar concerns. This work estimates these dimensions based on known characteristic sizes of PPS-1350 and a sectional view diagram of its magnetic circuit structure, employing proportional scaling measurements depicted in the figures. Naturally, such magnetic circuit dimensions lack precision; however, given that magnetic circuit optimization inherently involves automatic adjustment of the circuit structure under multiple constraints and the pursuit of a global optimal solution aided by algorithms, an initial deviation in the circuit that does not significantly impact the optimization outcome can be tolerated.

Now, we proceed to compute the scaling effects on the performance parameters of the thruster under this scaling regimen. According to Equation (17), the calculation yields $\lambda_T = T / T_0 = \sqrt{\lambda_U} \times \lambda_R^2 = 5.8$, indicating that the thrust increases from 89 mN to 516 mN. Subsequently, inserting $\lambda_T = 5.8$ into Equation (16) allows us to determine the mass flow rate scaling factor $\lambda_{\dot{m}} = \dot{m} / \dot{m}_0 = \lambda_T / \sqrt{\lambda_U} = 4.8$. At this point, utilizing Equation (10), we calculate $\lambda_B = B / B_0 = \lambda_{\dot{m}} / \lambda_R \lambda_W = 1.1$, implying a slight augmentation in the maximum magnetic field intensity post-scaling. Furthermore, guided by Equation (18), we find the specific impulse scaling factor to be $\lambda_{I_{sp}} \propto \sqrt{U_d} = 1.2$, signifying an enhancement from 1720 s to 2064 s.

3.2 Magnetic circuit optimization Settings

According to the principles of the selected scaling mode, the channel width expands to roughly twice that of the reference thruster. To maintain the relative density and distribution of magnetic field lines across the channel cross-section, it is necessary to correspondingly increase the magnetic induction intensity. When increasing the excitation input, the coil winding range is limited by the channel dimensions. Through adjustments, it was finally found that setting the excitation current to 4.5A, with an inner coil winding count of 260 turns and an outer coil winding count of 150 turns, satisfies the requirements of a 10kW Hall thruster. Both the inner and outer coil turn counts fall within their respective maximum winding limits, making this achievable.

The magnetic field constraints that guarantee stable operation of the reference thruster are as follows: Symmetry constraint, $\tan \theta \leq 0.1$, corresponds to an inclination angle not exceeding 6° [11,39-40]; Magnetic field gradient ∇B constraint, ranging from 90 to 120 G/cm [12,41]; Near-anode magnetic field intensity B_0 constraint, less than 3G [13]; B_r (max) constraint, ranging from 200 to 250G [14,42-43]; $L - B_m$ constraint, located 4 to 6mm behind the exit [44]. Since the magnetic field characteristics remain unchanged before and after scaling, the magnetic field requirements for the 10kW high-thrust Hall thruster are the same as above. The optimized constraint conditions are set out in Table 2. The magnetic circuit material is set to Q235 steel, and from its magnetization curve, it can be inferred that below 1.4T is the linear magnetization range of this material. Therefore, the upper limit for magnetic flux density is set to 1.4T, which corresponds to $B_{sat} \leq 1.4$.

TABLE 2 Summary of constraints for 10kW Hall thrusters

Constraint	Range
θ	Tangent value 0.1 (4 monitoring points)
∇B	80~150G/cm
B_0	Within 3G
B_r (max)	150~230G
$L - B_m$	Behind the exit 4~6mm
B_{sat}	Within 1.4T (6 monitoring points)

3.3 Magnetic circuit design effect analysis

The initial magnetic circuit's overall magnetic field morphology for the 10kW class Hall thruster is shown in Figure 7, and the overall magnetic field morphology after finite element optimization is shown in Figure 8, with a detailed comparison of the magnetic field inside the discharge channel depicted in Figure 9. It can be observed that the initial magnetic circuit retains some advantages of the dual-magnet screen structure, such as a certain magnetic field gradient and $(L - B_m)$ directing field lines outward along the plume path, as well as a smaller magnetic field intensity near the anode region. However, there are several inadequacies: poor symmetry of the magnetic field about the centerline, with a maximum magnetic tilt angle θ exceeding 20° ; an internal tilt angle reaching 9° at the channel exit; the magnetic field intensity and gradient might not meet actual requirements; and the allocation of magnetic circuit materials is not precise, leading to redundancy. Upon magnetic circuit optimization, it is clear that the magnetic field symmetry has significantly improved, with the average offset value of the magnetic line curvature center relative to the discharge channel decreasing from 5.3mm before optimization to 0.8mm afterwards. A convex magnetic field structure toward the anode is formed, creating a nearly zero-field zone along the central line in the vicinity of the anode (with magnetic field intensity values not exceeding 3 Gauss within a 5mm range before and after the anode). All aspects of the magnetic field requirements for the 10kW class Hall thruster have been effectively incorporated into the optimization process through constraints, and these requirements have been met following optimization

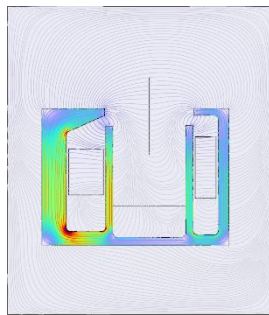


Fig.7 Overall magnetic field appearance of 10kW high thrust initial magnetic circuit

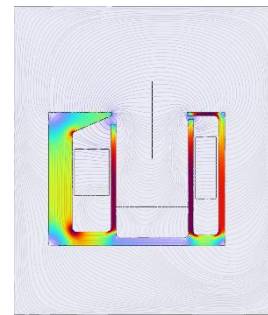


Fig.8 Overall magnetic field morphology after magnetic circuit optimization

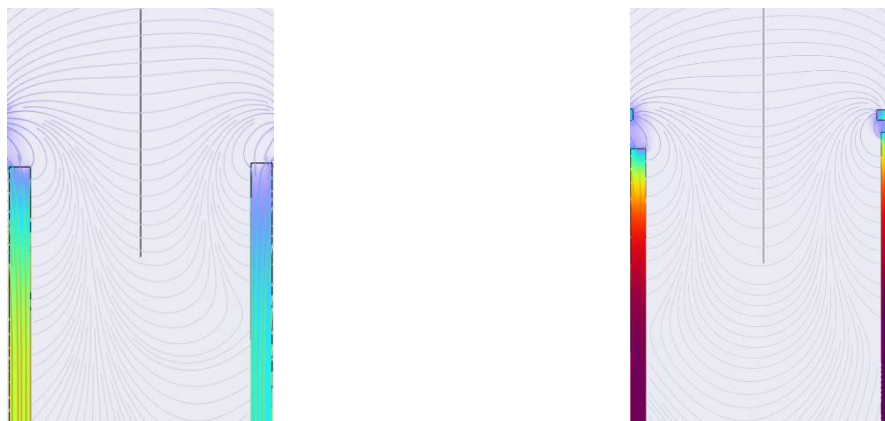


Fig.9 Optimize the magnetic field comparison of the front and rear channels

Due to the $B_r(\max)$ pushing outward along the plume direction and the gradual change of magnetic field intensity near the anode region, with the magnetic field gradient in the strong magnetic field region being the

focus of attention, in order to clearly analyze the variation of magnetic field intensity and visually reflect the changes in the magnetic field gradient, this paper extracts the magnetic field intensity along the central line within a range of 30mm in front of and 20mm behind the exit. A comparison of the central line magnetic field intensity before and after optimization is shown in Figure 10.

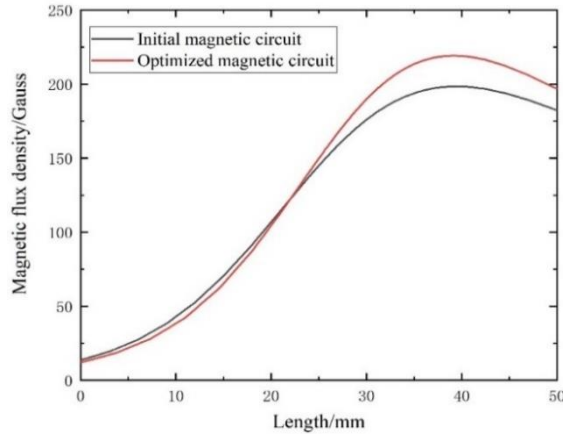


Fig.10 The magnetic field intensity comparison of the center line of the front and rear channels was optimized

The summary and comparison of constraint values before and after optimization are shown in Table 3.

TABLE 3 Comparison of constraints before and after optimization

Constraint	Initial Magnetic circuit	Optimized Magnetic circuit
θ	Above 20°	Within 6°
∇B	97.4G/cm	126.5G/cm
B_0	0.62G	0.84G
$B_r(\max)$	198.5G	219.3G
$L - B_m$	Behind the exit 5mm	Behind the exit 5mm
B_{sat}	Maximum is 1.20T	Maximum is 1.36T

From the results of the constraint values, the magnetic field gradient ∇B has increased by 19.6%, the maximum magnetic field intensity $B_r(\max)$ has increased by 10.5%, and the magnetic field intensity in the near-anode region B_0 has remained relatively unchanged, all within the range of the 3Gs constraint. Additionally, the distribution of the magnetic circuit material quality is more accurate after optimization, with the maximum magnetic flux $B_{sat}(\max)$ increasing from 1.20T to 1.36T; the axial position of the maximum magnetic field intensity $L - B_m$ remains at a distance of 5mm outside the channel, exhibiting the characteristics of a partially shielded magnetic configuration.

The before and after size comparison of the optimization is shown in Figure 11. Under the premise of ensuring that the material is in the linear magnetization working range, the size of the optimized magnetic circuit is effectively reduced compared to the initial model, reflecting the effective realization process of the optimization goal.

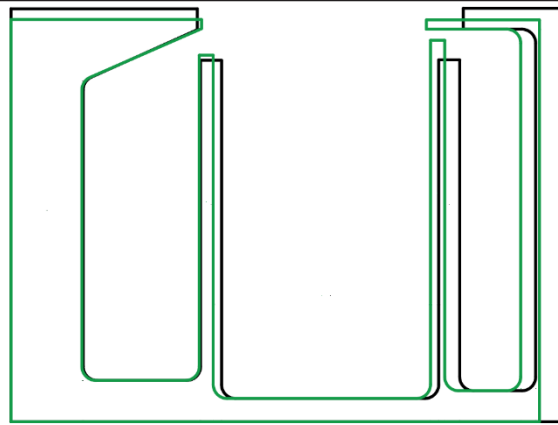


Fig.11 Optimize the size comparison between the magnetic circuit and the initial magnetic circuit (The green part is the optimized magnetic circuit)

It can be seen that after optimization, the gaps between the inner and outer magnetic poles, between the inner and outer magnetic poles and the magnetic screens have all decreased, which may also be one of the reasons for the increase in magnetic field gradient. The inner magnetic pole has slightly become thinner and longer, while the outer magnetic pole has become significantly thinner and longer. Both the inner and outer magnetic screens have undergone varying degrees of lengthening and thinning. The overall size has significantly reduced. Specifically, the thickness of the inner magnetic pole and its inner and outer sides has decreased by 6.6% and 125.0% respectively, with a slight increase in length, resulting in an overall weight reduction of 16.8%. The thickness of the outer magnetic pole has decreased by 125.1%, with an increase in length of 6.8%, resulting in an overall weight reduction of 109.6%. The thickness of the inner magnetic screen has decreased by 50.0%, with an increase in length of 2.42%. The thickness of the outer magnetic screen has decreased by 50.0%, with an increase in length of 5.53%. The thickness of the inner wall has decreased by 1.77%, and the thickness of the outer wall has decreased by 65.7%. After optimization, the total weight has been reduced by 24.6%.

4 Conclusion

This paper presents the magnetic circuit design for high-power Hall thrusters, including the design of a magnetic circuit for a 10 kW Hall thruster. Following finite element optimization, the refined magnetic circuit satisfies the requirements for high-power Hall thrusters in terms of magnetic field intensity, gradient, and topological configuration, yielding favorable outcomes. The study concludes as follows:

(1) Through scale-up methods, finite element optimization, and other techniques, this paper accomplishes the magnetic circuit design for Hall thrusters, providing technical support for the development of high-power Hall thrusters with broad application prospects.

(2) The 10 kW high-power Hall thruster designed based on scaling rules demonstrates a 480% increase in thrust and a 20% improvement in specific impulse compared to a medium-power reference thruster. Moreover, it permits the adjustment of discharge voltage and mass flow rate over a wider range than the reference thruster to attain desired levels of thrust and specific impulse.

(3) The magnetic circuit optimization efforts have proven effective, achieving a 24.6% reduction in magnetic circuit mass while reducing the maximum magnetic inclination angle from over 20° to within 6° , enhancing the maximum magnetic field strength by 10.5%, and boosting the magnetic field gradient by 19.6%, all while fulfilling specific criteria for magnetic field topology, strength, and gradient.

References:

- [1] Darnon F, Arrat D, d'Esquivan S, et al. Overview of electric propulsion activities in France[C]//43rd AIAA/ASME/SAE/ASEE Joint Propulsion Conference & Exhibit. 2005: 5165.
- [2] Rolfo A, Cadiou A, Secheresse O, et al. Plasma thrusters development in France[J]. *Acta Astronautica*, 2002, 51(1-9): 39-46.
- [3] Yu, D. Principles of space electric propulsion[M]. Harbin: Harbin Institute of Technology Press, 2014:23-45.
- [4] MOROZOV A I, BALEBANOV V M, BUGROVA A I, et al. ATON-thruster plasma accelerator[C]//The 4th All-Russian Seminar on Problems of Theoretical and Applied Electron Optics. Moscow: SPIE, 2000.
- [5] RATHSMAN P, KUGELBERG J, BODIN P, et al. SMART-1: development and lessons learnt[J]. *Acta Astronautica*, 2005, 57(2-8): 455-468.
- [6] Liu, Y, & Zhang, X. (Year). Research status and prospects of various thrust-level Hall thrusters. *Journal of Aerospace Power*, 37(12), 2782-2796.
- [7] Hargus Jr W A. Investigation of the plasma acceleration mechanism within a coaxial Hall thruster[M]. Stanford University, 2001.
- [8] Haas J M. Low perturbation interrogation of the internal and near-field plasma structure of a hall thruster using a high-speed probe positioning system[M]. University of Michigan, 2001.
- [9] Yu, S., Xu, Y., Zhang, Y., et al. (Year). Research progress and analysis of high-power Hall electric propulsion. *Chinese Journal of Space Science*, 42(2), 289-297.
- [10] Yu Bo, Huang Hao, Xu Yanan, et al. Study on the influence law of magnetic field on gas ionization rate of Hall thruster [J/OL]. *Propulsion Technology*, 1-13 [2024-03-19].
- [11] Barkalov E E, Veselovzorov A N, Pogorelov A A, et al. Composition of the beam of an SPT-100 stationary plasma thruster[J]. *Instruments and Experimental Techniques*, 2008, 51: 263-267.
- [12] Sankovic J M, Hamley J A, Haag T W. Performance evaluation of the Russian SPT-100 thruster at NASA LeRC[C]//IEPC Conference. 1994 (IEPC-93-094).
- [13] MacDonald-Tenenbaum N, Pratt Q, Nakles M, et al. Background pressure effects on ion velocity distributions in an SPT-100 Hall thruster[J]. *Journal of Propulsion and Power*, 2019, 35(2): 403-412.
- [14] Steven R O, John M S. Advanced Hall electric propulsion for future in-space transportation[C]//3rd International Spacecraft Propulsion Conference, Cannes, France. 2000.
- [15] Darnon F, Arrat D, d'Esquivan S, et al. Overview of electric propulsion activities in France[C]//43rd AIAA/ASME/SAE/ASEE Joint Propulsion Conference & Exhibit. 2005: 5165.
- [16] Gascon N, Dudeck M, Barral S. Wall material effects in stationary plasma thrusters. I. Parametric studies of an SPT-100[J]. *Physics of Plasmas*, 2003, 10(10): 4123-4136.
- [17] Barral S, Makowski K, Peradzyński Z, et al. Wall material effects in stationary plasma thrusters. II. Near-wall and in-wall conductivity[J]. *Physics of Plasmas*, 2003, 10(10): 4137-4152.
- [18] Rolfo A, Cadiou A, Secheresse O, et al. Plasma thrusters development in France[J]. *Acta Astronautica*, 2002, 51(1-9): 39-46.
- [19] Rossetti P, Casaregola C, Andrenucci M. 30 kW-Class Hall Thruster: a Key Building Block for Propulsion Needs of Future Space Transportation and Exploration[C]//32nd International Electric Propulsion Conference, IEPC-2011-211. 2011.
- [20] Szabo J, Pote B, Byrne L, et al. Eight Kilowatt Hall thruster system characterization[C]//33rd International Electric Propulsion Conference, Washington, DC, United States. 2013: 1-8.
- [21] Szabo J, Pote B, Hruby V, et al. A commercial one Newton Hall effect thruster for high-power in-space missions[C]//47th AIAA/ASME/SAE/ASEE Joint Propulsion Conference & Exhibit. 2011: 6152.

- [22] Hofer R R, Cusson S E, Lobbia R B, et al. The H9 magnetically shielded Hall thruster[C]//35th International Electric Propulsion Conference. Electric Rocket Propulsion Soc., 2017: 2017-232.
- [23] Kamhawi H, Huang W, Haag T, et al. Performance and thermal characterization of the NASA-300MS 20 kW hall effect thruster[C]//International Electric Propulsion Conference (IEPC 2013). 2013 (GRC-E-DAA-TN11609).
- [24] Kamhawi H, Haag T W, Jacobson D T, et al. Performance evaluation of the NASA-300M 20 kW Hall effect thruster[J]. AIAA Paper, 2011, 5521: 2011.
- [25] Hofer R R. Development and characterization of high-efficiency, high-specific impulse xenon Hall thrusters[M]. University of Michigan, 2004.
- [26] Katz I, Lopez Ortega A, Goebel D, et al. Performance and Facility Background Pressure Characterization Tests of NASA's 12.5-kW Hall Effect Rocket with Magnetic Shielding Thruster[C]//14th Spacecraft Charging Technology Conference, ESA/ESTEC. 2016.
- [27] Kamhawi H, Huang W, Haag T, et al. Performance, Facility Pressure Effects, and Stability Characterization Tests of NASA's Hall Effect Rocket with Magnetic Shielding Thruster[C]//AIAA/SAE/ASEE Joint Propulsion Conference. 2016 (GRC-E-DAA-TN33862).
- [28] TU Z H, MAO W, HU Y L, et al. Magnetic circuit design method based on size optimization in Hall thrusters [J]. Aerospace Control and Application, 2024, 50 (1): 117-126 (in Chinese).
- [29] MANZELLA D H, JACOBSON D T, JANKOVSKY R S, et al. Magnetic circuit for Hall effect plasma accelerator[P]. U.S. Patent: 7,624,566, 2009-12-1.
- [30] Dannenmayer K, Mazouffre S. Elementary scaling laws for sizing up and down Hall effect thrusters: Impact of simplifying assumptions[C]//Proceedings of the 31st International Electric Propulsion Conference (Ann Arbor), IEPC. 2009: 09-077.
- [31] Dannenmayer K, Mazouffre S. Elementary scaling relations for Hall effect thrusters[J]. Journal of Propulsion and Power, 2011, 27(1): 236-245.
- [32] Daren Y, Yongjie D, Zhi Z. Improvement on the scaling theory of the stationary plasma thruster[J]. Journal of Propulsion and Power, 2005, 21(1): 139-143.
- [33] Zhurin V V, Kaufman H R, Robinson R S. Physics of closed drift thrusters[J]. Plasma Sources Science and Technology, 1999, 8(1): R1.
- [34] Khayms V, Martinez-Sanchez M. Design of a miniaturized Hall thruster for microsattellites[C]//32nd Joint Propulsion Conference and Exhibit. 1996: 3291.
- [35] ROSSI A, MESSINE F, HÉNAUX C. Parametric optimization of a Hall effect thruster magnetic circuit[J]. Aerospace Technology Japan, 2016, 14(30): 197-202.
- [36] Xu Zongqi, Tian Leichao, Wang Pingyang, et al. Simulation study on the influence of magnetic shield size on the performance of Hall thruster [J]. Chinese Journal of Space Science and Technology, 2023, 43(04): 43-51.
- [37] REZA M, FERRATO E, FARAJI F, et al. Magnetic circuit optimization for Hall thrusters design[C]//The 36th International Electric Propulsion Conference. Vienna: University of Vienna, 2019.
- [38] LAURENT B, ROSSI A, ÖBERG M, et al. High throughput 1.5 kW Hall thruster for Satcoms[C]//The 36th International Electric Propulsion Conference. Vienna: University of Vienna, 2019.
- [39] RICHARD R H, ROBERTS J. The influence of current density and magnetic field topography in optimizing the performance, divergence, and plasma oscillations of high specific impulse Hall thrusters[C]. //The 28th International Electric Propulsion Conference. Toulouse: AIAA, 2003.
- [40] RICHARD R H, ALEC D, GALLIMORE. The role of magnetic field topography in improving the performance of a high

voltage Hall thruster[C]//The 38th Joint Propulsion Conference & Exhibit. Washington D.C.: AIAA, 2002.

- [41] E Peng. Study on the influence of magnetic field inside the channel of Hall thruster on discharge characteristics [D]. Harbin: Harbin Institute of Technology, 2009.
- [42] KEIDAR M, BOYD I D. On the magnetic mirror effect in Hall thrusters[J]. Applied Physics Letters, 2005, 87(12):121501.
- [43] GAWRON D, MAZOUFFRE S, SADEGHI N, et al. Influence of magnetic field and discharge voltage on the acceleration layer features in a Hall effect thruster[J]. Plasma Sources Science and Technology, 2008, 17(2): 025001.
- [44] MAO W, WU N, HU Y L, et al. Life test research of a high specific impulse Hall thruster HEP-140MF[J]. Plasma Science and Technology,2020,22(09):157-166.